J Porous Mater (2017) 24:1363–1373
DOI 10.1007/s10934-017-0378-1

One-step synthesis of nitrogen-doped porous carbon for high performance supercapacitors

Jian-Qiang Zhang[1] · Ping Li[1] · Si-Yun Huang[1] · Bin Wang[1] · He-Ming Luo[1]

Published online: 2 February 2017

Abstract We report a simple synthesis of nitrogen-doped porous carbon materials by one-step carbonization of pure sodium glutamate in inert atmosphere without any activation. The surface area, pore structure, and electrochemical properties of the resultant carbon materials can be tuned simply by changing the carbonization temperature. The carbon materials are characterized by heteroatom (N, O) doping, interconnected porous carbons framework with high surface area (1873 m^2 g^{-1}), large pore volume (1.10 cm^3 g^{-1}), and high yield. While the nitrogen content decreases from 7.15 at% at 600 °C to 4.03 at% at 900 °C. These features confer the as-obtained nitrogen-doped porous-carbon materials with high specific capacitance, good rate capability, and excellent cycling stability (88.15% of capacitance retention after 5000 cycles) in 2 M $NaNO_3$ electrolyte.

Keywords Nitrogen-doped porous carbon · Supercapacitors · Specific capacitance · $NaNO_3$ electrolyte

1 Introduction

Supercapacitors, also known as electrochemical double layer capacitors (EDLCs) or pseudo-capacitors, are attracting increased attention because of their high power density and long cycle life [1, 2]. Carbon has various allotropes and different degrees of graphitization, which yield several microstructures in many forms and variety of dimensionality [3–5]. Therefore, carbon materials are considered to be the most promising electrode materials for supercapacitors.

However, the main limitation of supercapacitors is their lower energy density than batteries, as well as their high cost per unit energy [6, 7]. To achieve high energy density in supercapacitors, the capacitance of each electrode should be maximized, and the maximum allowed operational voltage of supercapacitor should be increased. However, porous-carbon materials have a low capacitance, which is related to the total charge amount accumulated at the electrode/electrolyte interface [8]. Capacitance may be improved by using redox-active electrolytes or by providing additional charge originating from faradaic reactions, which can increase electrode capacitance. Electrode materials providing pseudo-capacitance are mainly composed of transition-metal oxides such as Mn-based [9–11], Vanadium-based [12], Co_3O_4 [13], and NiO [14] and may be assembled both as pure materials in asymmetric configuration, e.g., with carbon electrode [15]. However, low conductivity, poor cycle stability, and high cost limit the practical application of pseudo-capacitive materials.

Other promising materials providing pseudo-capacitance are carbon materials enriched by heteroatoms such as oxygen or nitrogen [16, 17]. In these materials pseudo-capacitance originates from redox reactions of functional groups and from local changes in the electron density of a carbon matrix being enriched by a heteroatom [18, 19]. The incorporation of nitrogen into the carbon network can be achieved by two strategies, i.e., by post-treatment of carbons or by using nitrogen-containing precursors. In the former, carbon materials are post-treated with ammonia, amine, or urea to introduce nitrogen-containing functional groups on their surface [20–24], which does not change the properties of the bulk material. In the latter, in situ doping

✉ He-Ming Luo
luohm666@163.com

[1] College of Petrochemical Technology, Lanzhou University of Technology, Lanzhou 730050, China

using various nitrogen-containing precursors is performed to enable homogeneous incorporation of nitrogen into carbon materials with controlled chemistry. Various nitrogen-containing precursors have been widely investigated to prepare nitrogen-doped porous carbons, including synthetic polymers [21, 25–27], biomass or biomass derivatives [28–30], small organic molecules [31], and ionic liquid [32, 33]. The relevant approaches include carbonization–activation method, template, and polymer blend. Most recently, nitrogen-doped porous-carbon materials have been synthesized by an easy one-step carbonization of nitrogen-containing precursors, such as tetrasodium salt of ethylenediamine tetraacetic acid [34], ethylenediamine tetraacetic acid disodium magnesium salt [35], 3-methyl-1-butylpyridine and dicyanamide [32]. These works suggest that nitrogen-containing organic salts can be used as precursors for nitrogen-doped carbons. However, the development of nitrogen-doped porous carbons by using cost-effective materials and sample synthesis is still highly demanded to realize the commercial applications of electrode materials in supercapacitors.

Sodium glutamate is a kind of seasoning whose main content is sodium (2S)-2-amino-5-hydroxy-5-*oxo*-pentanoate. Sodium glutamate is used as a low-cost, environmentally friendly nitrogen-containing carbon source because it is easily derived from plant residues. The present paper reports a single-step synthesis of new nitrogen-doped porous-carbon materials through monosodium-glutamate carbonization. Neutral electrolytes render the EDLC assembly process simple and economic because of their favorable properties, including cost effectiveness, corrosion resistance, electrochemical stability, environmental friendliness, and compatibility with diverse current collectors. The performance of the materials as electrodes for supercapacitors is evaluated in 6 M KOH solution and 2 M $NaNO_3$ aqueous solution.

2 Experimental

2.1 Synthesis of materials

Pure monosodium glutamate (Sodium glutamate: $C_5H_8O_4NNa{\cdot}H_2O$) was purchased commercially. Nitrogen-doped porous carbon materials were prepared by direct carbonization of sodium glutamate. The prepared sodium glutamate was ground, placed in a porcelain boat, and further heated in a horizontal tube furnace up to 600, 700, 800, or 900 °C at a rate of 3 °C min^{-1}. The last temperature was maintained for 2 h under N_2 (99.999%) flow. Subsequently, the resulting black substance was washed with 1 M HCl solution to remove inorganic impurities and then with deionized water until pH was neutral. After filtration, the product was dried at 80 °C. The nitrogen-doped porous carbons were named CMG-T, where MG means monosodium glutamate and T means carbonization temperature.

2.2 Yield of materials

The yield of CMG-800 is ~16%. Specifically, the carbon conversion rate of sodium glutamate exceeded 40%. The yield of CMG-T is listed in Table 1.

2.3 Structural characterizations

Powder X-ray diffraction (XRD) patterns in the Bragg's angle (2θ) range of 5°–90° were collected using a D/Max-2400 (Rigaku) diffractometer with monochromatic Cu $K\alpha$ radiation of wavelength $\lambda = 0.1541$ nm at a scanning speed of 15° min. Raman spectra were recorded using a Horiva (JY-HR800 micro Raman) spectrometer. The excitation source is a laser at 532 nm with 25 mW power. The morphology of the nitrogen-doped porous carbons was investigated by field-emission scanning electron microscopy (SEM; JSM-5600LV, JEOL) and high-resolution transmission electron microscopy (HRTEM; JEM-1200EX, JEOL). Surface elemental composition was determined by X-ray photoelectron spectroscopy (XPS) using a VG scientific ESCA-3000 spectrometer with non-monochromatized

Table 1 Yield of nitrogen-doped porous carbon samples

Organic salt	Carbon content (wt%)	Sample	Carbon conversion (%)[a]	Yield (%)[b]
Monosodium glutamate $C_5H_8O_4NNa{\cdot}H_2O$	35.48	CMG-600	27.76	9.14
		CMG-700	46.81	16.61
		CMG-800	46.56	16.52
		CMG-900	44.33	15.73

[a] $\alpha = (W_i / (W \times 47.05\%)) \times 100\%$

[b] $Y = (W_i/W) \times 100\%$, where α is carbon conversion in the organic salt, Y is the yield, W_i is the weight of carbon materials, and W is the weight of the initial material

Mg *K*α radiation (1253.6 eV). The structure performance of the nitrogen-doped porous carbons was measured through nitrogen sorption isotherms obtained using a Micromeritics ASAP 2020 sorptometer. The apparent surface area (S_{BET}) was calculated from the N_2 isotherms at relative pressures (P/P_o) from 0.06 to 0.20 through the Brunauer–Emmett–Teller (BET) method [36, 37].

2.4 Electrochemical measurements

To prepare the working electrode, nitrogen-doped porous carbon materials were ground with super P (15 wt%) and polytetrafluoroethylene (5 wt%) and then pressed onto nickel foam (1 cm^2) functioning as current collector. The total material loading on each electrode was approximately 5 mg. These carbons were then dried in a vacuum at 80 °C for 12 h. Subsequently, the working electrode was pressed at 15 MPa for 1 min.

Electrochemical measurements including cyclic voltammetry (CV), galvanostatic charge–discharge (GCD), and electrochemical impedance spectroscopy (EIS) were performed in 6 M KOH and 2 M $NaNO_3$ aqueous solution by using a three-electrode system with the nitrogen-doped porous carbon materials as the working electrode, a platinum slice (~1.5 cm^2) as the counter electrode, and a saturated calomel electrode (SCE) as the reference electrode. GCD tests were performed at different currents densities over a potential window of −1–0 V. Specific capacitance C (F g^{-1}) was calculated as shown in Eq. (1):

$$C = \frac{I \cdot \Delta t}{m \cdot \Delta V} \tag{1}$$

where I is the constant discharging current (A), Δt is the discharge time (s) for the potential change ΔV (V), and m (g) is the mass of the nitrogen-doped porous-carbon materials in the electrode.

CV was performed at different scan rates over the potential window of −1–0 V. Specific capacitance C (F g^{-1}) was also calculated from the CV curves according to Eq. (2):

$$C = \frac{\int i(V)dV}{2 \cdot vm\Delta V} \tag{2}$$

where i(V) is the current as the function of voltage, and ν is the scan rate (V s^{-1}).

EIS measurements were performed at open-circuit potential with an AC amplitude of 5 mV within the frequency range of 10^{-2}–10^5 Hz.

3 Results and discussion

3.1 Structural characteristics of nitrogen-doped porous carbons

XRD and Raman spectroscopy characterizations were conducted to obtain phase-structure information about the CMG-800 samples, as shown in Fig. 1. Figure 1a shows the XRD patterns of CMG-T samples. All samples demonstrate two broad diffraction peaks centered at 2θ of approximately 25° and 44° in their XRD patterns, which are approximately indexed as the (002) and (101) planes of graphite, respectively. The XRD patterns displayed a broad peak at 2$\theta \approx 25.08°$, which was approximately indexed as the (002) planes of graphite (2$\theta \approx 26.6°$), with an expanded interlayer spacing of 0.4 nm compared with that of graphite (0.334 nm) [38, 39]. This finding suggested the presence of disordered or amorphous carbon. With increased carbonization temperature, the (002) diffraction peaks shifted to higher angles, suggesting decrease of the average carbon-to-carbon distance in the as-synthesized carbon materials with increased carbonization temperature.

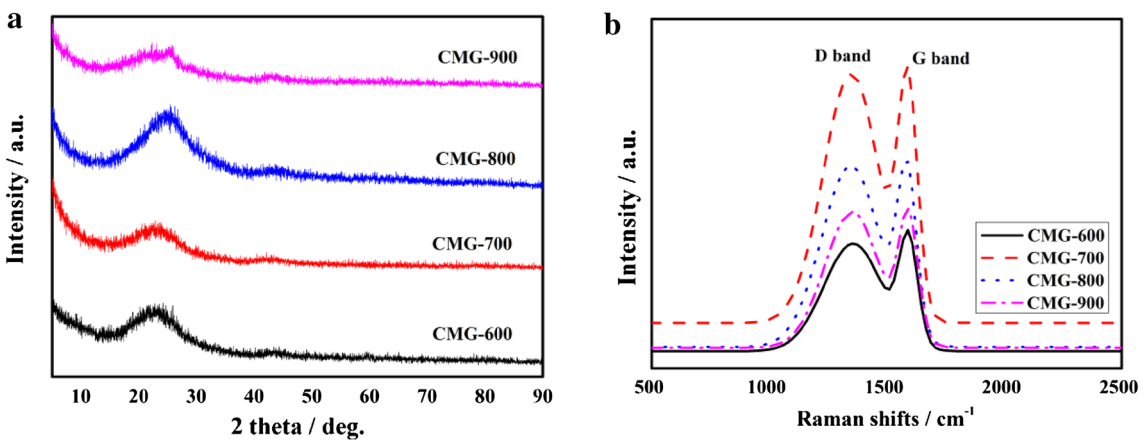

Fig. 1 **a** XRD patterns, **b** Raman spectra of CMG-T samples

The Raman spectra of the CMG-800 sample are shown in Fig. 1b, and two characteristic peaks centered at approximately 1347.1 (D-band) and 1589.1 (G-band) cm^{-1} were observed. The D-band stood for the disorder induced mode related to structural defects and imperfections [40], whereas the G-band originated from the E_{2g} phonon vibrations of sp^2 carbon atoms [41]. The position, intensity, and broadening of the D band (relative to the G band) depended on the structure and uniformity of the disordered carbon, as well as the presence of functional groups [42]. The CMG-T samples exhibited a strong D band signal and a slightly less intense G band with an I_D/I_G intensity ratio less than 1, which showed that structurally disordered carbons was formed. The full-width at half-maximum of both the G bands and D bands decreases with the increase of carbonization temperature, suggesting a structurally disordered carbon formed at a relatively low temperature.

SEM images of CMG-800 sample exhibited architecture with macroscopic pores interconnected with one another, as shown in Fig. 2a. Further high-resolution SEM analysis (Fig. 2b) showed that CMG-800 sample had an interconnected pore structure. To obtain the intrinsic structure of carbon, HRTEM was also used, as shown in Fig. 2a, 2b. HRTEM images of CMG-800 sample demonstrated that the pore walls consisted of many randomly distributed mesopores. These pore structure facilitated rapid ion diffusion, ion buffering, and ion storage, thereby guaranteeing full surface-area utilization.

The surface functional groups of CMG-T samples were identified by XPS (Figs. 3, 4). As shown in Fig. 4, three strong peaks within the range of 250–550 eV corresponded to C*1s*, N*1s*, and O*1s*, respectively, in agreement with their corresponding element mapping images, suggesting the successful formation of nitrogen-doped porous-carbon materials after sodium glutamate carbonization. The corresponding high-resolution spectrum of N*1s* in all the samples after deconvolution using four peaks is shown in Figs. 3a and 4b. The strongest peak, with a binding energy centered at 400.1 eV, was due to pyrrolic-N, and the other peaks centered at 398.5, 401.2, and 404.0 eV could be due to pyridinic-N (N-6), quaternary-N (N-Q), and pyridine-N-oxide species (N-x), respectively [43–45]. Among these four different nitrogen configurations, N-6 and N-5 were assumed to be the main configurations contributing to the

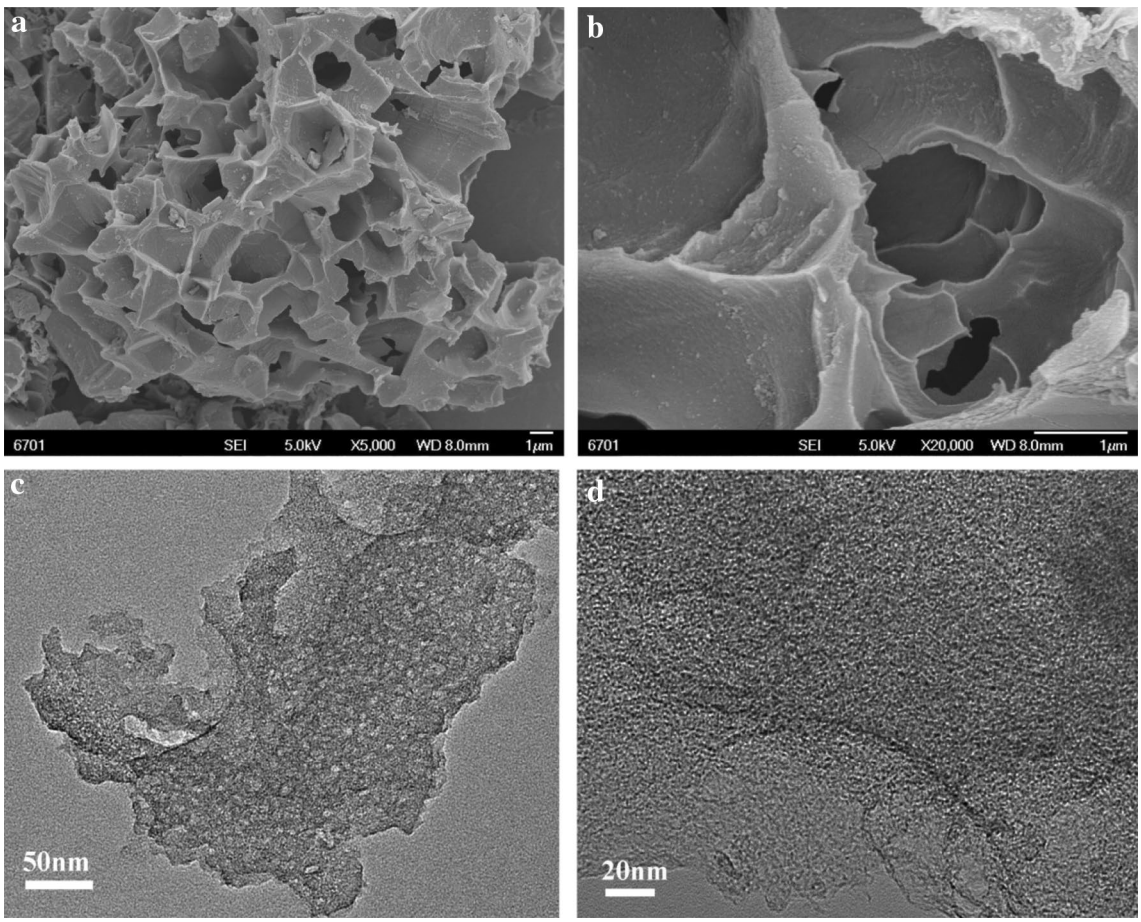

Fig. 2 SEM images: **a** ×5000, **b** ×20,000, HRTEM images: **c** 50 nm, **d** 20 nm of CMG-800 sample

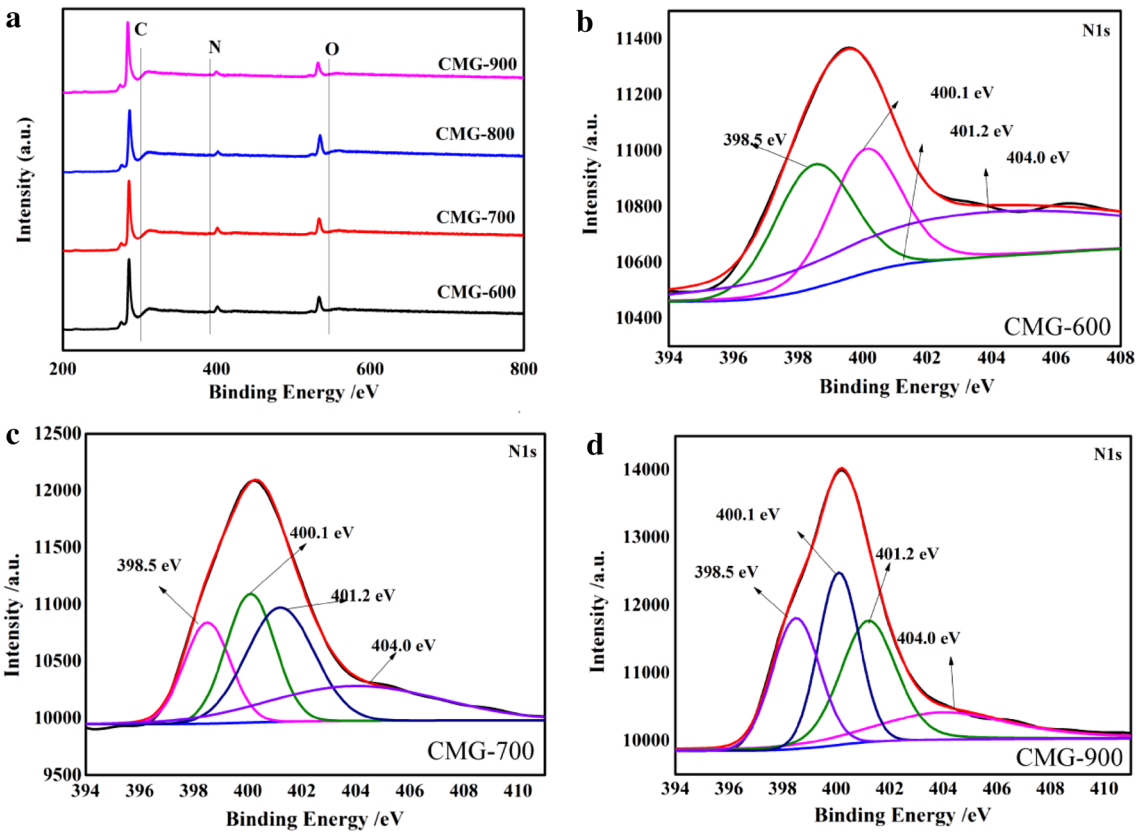

Fig. 3 **a** XPS survey, N*1s* XPS spectra of **b** CMG-600, **c** CMG-700, and **d** CMG-900 sample

faradaic reaction-based pseudocapacitance [46]. Introducing nitrogen into the porous carbon electrodes can also change the electron distribution of the materials, which can further enhance wettability between electrolytes and electrode materials, leading to increased active surface area accessible to the electrolyte [47]. Based on the intensity of XPS peaks, the fractions of these different types of N and O atoms are calculated, as listed in Table 2. The concentrations of N and O atoms decreased with increasing carbonization temperature. The N atoms content in CMG-600 sample is 7.15at%. As the carbonization temperature increases to 700 °C, the N atoms content decreases to 5.33at%.

The four peaks fitted in C*1s* spectrum (Fig. 3a) corresponded to C=C (284.7 eV), C–N and/or C=N (285.2 eV) [48], C–O (286.4 eV), and O–C=O (289.4 eV) [49, 50]. Two peaks in the O1s spectrum (Fig. 3d) were positioned at 531.3, 532.5, and 533.4 eV, which corresponded to –C=O(ester), –C=O(carboxyl), and O–C=O, respectively [51]. The concentration of O atoms in samples decreases in the order of 10.79 at% at 600 °C > 9.32at% at 700 °C > 8.75 at% at 800 °C > 4.91at% at 900 °C.

The porous structure of the nitrogen-doped porous-carbon materials obtained from the nitrogen-sorption isotherms is shown in Fig. 5. The nitrogen sorption isotherm of CMG-700, CMG-800 and CMG-900 samples are type IV according to the IUPAC classification [52], indicating that the pores were mainly mesopores, which benefited ion storage during charge–discharge process. The adsorbed N_2 volume significantly increased at low pressure (approached 0), which implied that the amount of micropores in carbon was not negligible. The hysteresis loop observed at moderate pressure (0.45–1) revealed the presence of slit-shaped mesopores in the carbon. The nitrogen sorption isotherm of CMG-600 sample is type I, which indicates that the material mainly contains micropores. Figure 5b shows the corresponding pore-size distribution plots of the various nitrogen-doped porous-carbon materials obtained using DFT based on the adsorption branch of the N_2 isotherms. The pore-size distribution of CMG-800 sample showed considerable mesopores with sizes of 2–5 nm (Fig. 5b). A clear hierarchical pore structure containing mesopores was found in CMG-800 sample. Compared with those of CMG-600 sample and CMG-700 sample, the pore volume of CMG-800 sample increased mainly because of the appearance of mesopores. Interestingly, the pore distribution of the CMG-900 sample was similar to that of the CMG-800 sample, but CMG-900 sample showed a much lower mesopore volume. This decrease could be related to carbonization

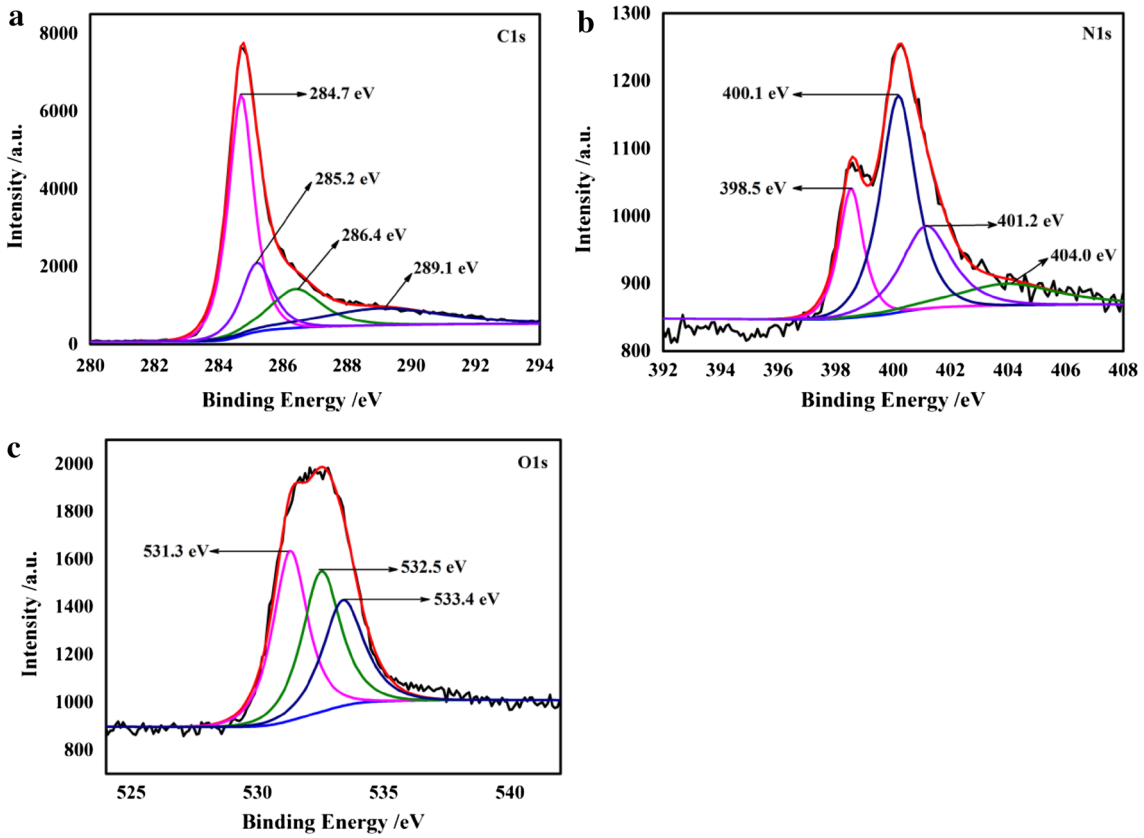

Fig. 4 **a** C *1 s*, **b** N *1 s*, and **c** O *1 s* XPS spectra of CMG-800 sample after fitting

Table 2 Textural properties of the nitrogen-doped porous carbon samples obtained at different carbonization conditions

Sample	S_{BET} ($m^2\ g^{-1}$)	Pore volume ($cm^3\ g^{-1}$)[a]	Micropore volume ($cm^3\ g^{-1}$)[b]	Average pore sizes (nm)
CMG-600	640	0.24	0.12	2.0
CMG-700	865	0.34	0.06	2.1
CMG-800	1873	1.10	0.22	2.3
CMG-900	1193	0.68	0.19	2.4

[a]Pore volume at p/p_o ~0.97

[b]Micropore volume determined by the *t*-plot technique

temperature. Results indicated that CMG-800 sample demonstrated the optimal microstructure and porosity with a hierarchically porous structure that was rich in micropores and mesopores.

The textural parameters of nitrogen-doped porous-carbon materials are listed in Table 2. The nitrogen-doped porous-carbon materials had large specific BET surface areas with wide ranges, i.e., between 640 $m^2\ g^{-1}$ for CMG-600 sample and 1873 $m^2\ g^{-1}$ for CMG-800 sample. Similarly, the pore volumes of nitrogen-doped porous carbon were 0.24 $cm^3\ g^{-1}$ for CMG-600 sample and 1.10 $cm^3\ g^{-1}$ for CMG-800 sample. These results revealed that the textural properties of nitrogen-doped porous-carbon materials significantly depended on carbonization temperature.

3.2 Electrochemical performance

3.2.1 Electrochemical performance in 6 M KOH solutions

The impact of carbonization temperature on the electrochemical performance of nitrogen-doped porous carbon was investigated. As shown in the Fig. 6, The optimal electrochemical properties of the nitrogen-doped porous carbon materials showed that the carbonization temperature of 800 °C, which resulted in microstructural formation, was more favorable for the transport of electrolyte ions than the carbonization temperatures of 600, 700, and 900 °C. CMG-800 sample obviously showed the best electrochemical behaviors among the materials studied. Study shows that the ions diffuse slowly in macropores because of diffusion kinetics [53]. That is, the ions easily experience a "traffic jam" in the macropores, which consequently increases the resistance. In addition,The specific capacitances of CMG-600 and CMG-700 samples were lower than that of CMG-800 sample. In general, the sub-micropores of the materials

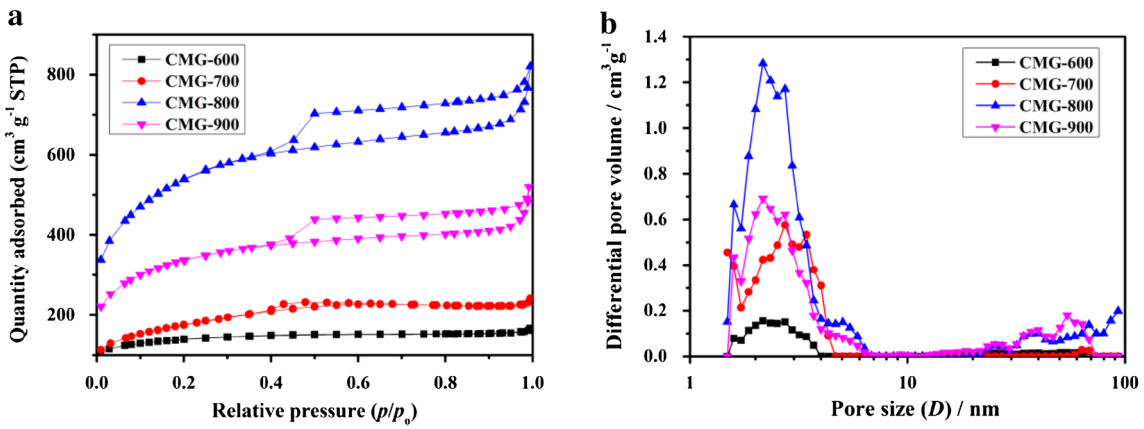

Fig. 5 **a** N_2 adsorption/desorption isotherm, **b** the pore size distribution of CMG-T samples

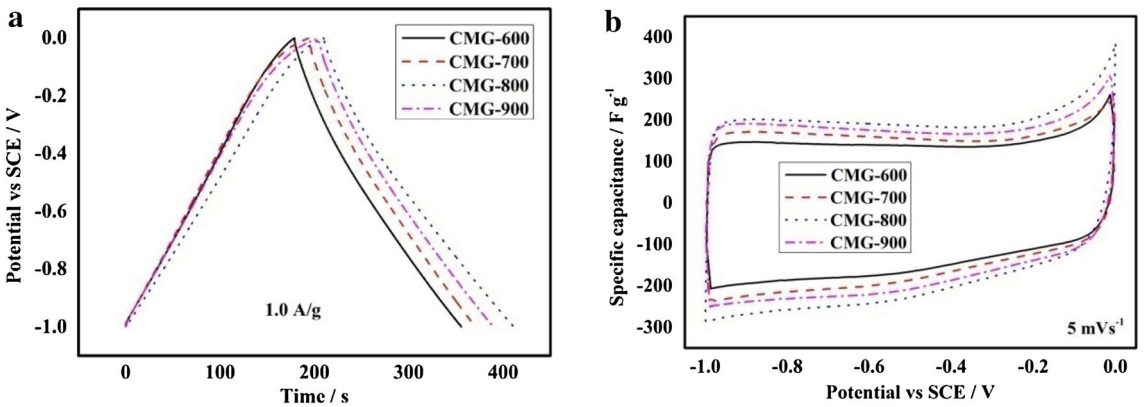

Fig. 6 CMG-T samples: **a** GCD curves at 1.0 A g^{-1} **b** CV curves at 5 mV s^{-1}

do not participate in super-capacitance formation because of the in accessibility of sub-micropore surfaces to large solvated ions [54].

Figure 7 displays the Nyquist plots of CMG-T samples. The AC-ESRs of CMG-600, CMG-700, CMG-800, and CMG-900 samples were 0.627, 0.598, 0.543 and 0.573 Ω, respectively. Clearly, CMG-800 sample had the smallest pseudo-charge-transfer resistance among the carbon materials. This finding can be mainly attributed to the maximized access of electrolyte ions to a greater number of pores in the carbon material at low frequencies, in contrast to the limited penetration of electrolyte ions at high frequencies, which only reached the pores at the surface of the electrode/electrolyte interface.

Figure 8a demonstrates the GCD curves of CMG-800 sample measured at different current densities from 1 to 20 A g^{-1}. As expected, the discharge curves of CMG-800 sample were nearly symmetric with the corresponding charge curves. These indicate the reversible adsorption/desorption of ions, which suggests that electrochemical

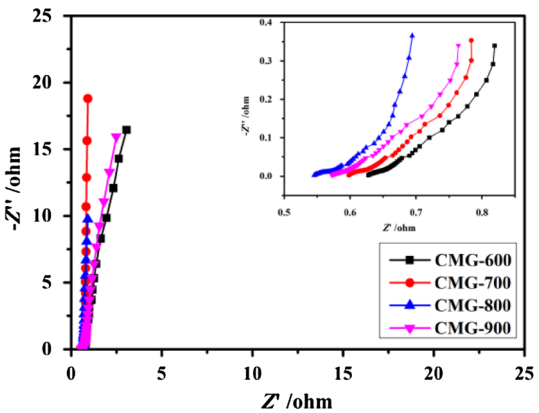

Fig. 7 Nyquist plot for CMG-T samples in 6 M KOH (*Inset* shows the same in the higher frequency region)

contributions originate from EDLC and that a slight pseudo-capacitance are observed. The observed increase in specific capacitance from 143 F g^{-1} (20 A g^{-1}) to

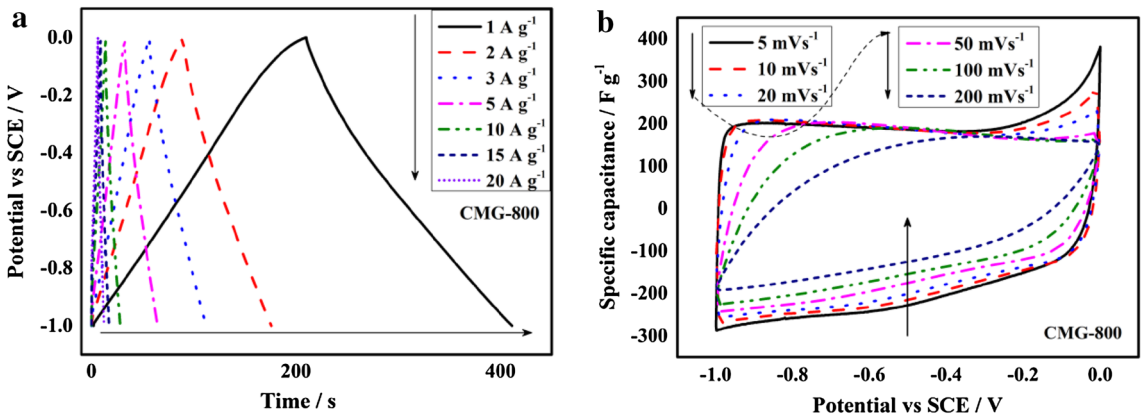

Fig. 8 **a** GCD curves **b** CV curves of CMG-800 sample in 6 M KOH

205 F g^{-1} (1 A g^{-1}) was possibly due to the diffusion limitation within the micropores in the carbon material of CMG-800 sample. This result are larger than some previous reported carbon materials such as coconut kernel-derived activated carbon (173 F g^{-1} at 0.25 A g^{-1}) [55], attapulgite/maltose system on mesopore carbon materials(171 F g^{-1} at 0.6 A g^{-1}) [56], and mesoporous-activated carbon spheres (204 F g^{-1} at 0.5 A g^{-1}) [57]. Figure 8b shows the CV curves of CMG-800 sample in 6 M KOH electrolyte at different scan rates within the potential window ranging from −1 to 0 V. All CV curves exhibited a nearly rectangular shape, indicating the formation of an EDLC at the electrode–electrolyte interface. The small reduction–oxidation humps and peaks observed in the CV curves originated from the oxygen- and nitrogen-containing functional groups remaining in the carbon samples. This result indicated that the revisable redox reactions of oxygen- and nitrogen-containing functional groups induced the extra pseudo-capacitance that improved the specific capacitance [58]. The current responses of CMG-800 sample showed a slight scan rate dependence. Only the accessible surface area contributed to specific capacitance; thus, the specific capacitance may have been contributed by the meso/macropores of the nitrogen-doped porous carbons at high scan rates and by micropores at low scan rates. The quasi-rectangular shape was maintained for the CV curves even at a very high scan rate, demonstrating excellent electrochemical behavior and implying the stability of its unique porosity characteristics and surface oxygen- and nitrogen-containing functional groups. The specific capacitance of CMG-800 sample decayed by 30.84% (from 201 to 139 F g^{-1}) with increased scan rate from 5 to 200 mV s^{-1}, indicating their excellent porosity characteristics, in agreement with the pore-size distribution analysis.

The cyclic stability of CMG-800 sample was measured at a constant discharge current density of 2 A g^{-1}. A high capacitance retention of 93.22% was obtained even after charging–discharging for 5000 times, as shown in Fig. 9a. The coulombic efficiency stays above 99.2% during cycle. The high cycling durability of CMG-800 sample after 5000 cycles was believed to be related to its large BET surface area and optimal microstructure.

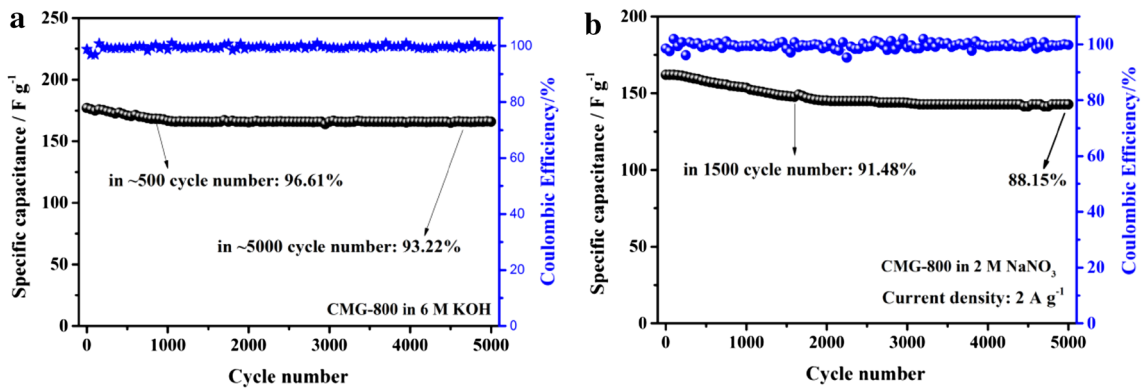

Fig. 9 Cyclic stability of CMG-800 sample in: **a** 6 M KOH solution, and **b** 2 M $NaNO_3$ solution

3.2.2 *Electrochemical performance in 2 M $NaNO_3$ solutions*

Neutral electrolytes rendered simple and economical the supercapacitor assembly process because of their favorable properties, including cost effectiveness, corrosion resistance, electrochemical stability, environmental friendliness, and compatibility with diverse current collectors. Thus, the performance of CMG-800 sample as a supercapacitor electrode component was evaluated in $NaNO_3$ aqueous solution. The CVs for different scan rates in 2 M $NaNO_3$ electrolyte are given in the Fig. 10a. The corresponding CV curve of CMG-800 sample demonstrated an irregular rectangular shape with hump peak at low potential, again suggesting the presence of a pseudocapacitive contribution beyond the electrical double-layer capacitive contribution because of the presence of oxygen- and nitrogen-containing functional groups. At higher scan rates, the CV curve was distorted because of the diffusion limitation within the carbon material of CMG-800 sample and the higher electrolyte resistance than that of KOH electrolyte. The highest specific capacitance of 165 F g^{-1} was achieved at 5 mV s^{-1}, maintained at 120 F g^{-1} and 100 mV s^{-1}. Figure 10b represents the GCD measurements for different current densities. The GCD curves of the CMG-800 sample were not straight lines and showed distortion, suggesting the presence of pseudocapacitive behavior caused by the oxygen- and nitrogen-containing functional groups. The highest specific capacitance of 174 F g^{-1} was achieved at 1 A g^{-1}, maintained at 126 F g^{-1} and 20 A g^{-1}. About 72.41% capacitance was retained when the charging current was increased 20 times. A high specific capacitance retention of 93.22% (with an average coulombic effifiency of >98%) was obtained even after charging–discharging 5000 times, as shown in Fig. 9b.Compared with that of KOH electrolyte, $NaNO_3$ electrolyte exhibited a low specific capacitance, which can be primarily explained by the poor conductivity of the solutions and the steric hindrance caused by hydrated molecules.

Figure 11 shows the Nyquist plots for the 6 M KOH and 2 M $NaNO_3$ electrolyte. In the low-frequency region, the vertical nature of the Nyquist plots clearly indicates the capacitive behaviour of the CMG-800 sample [59]. The Nyquist plot expanded in the high-frequency region is shown in the inset. The intercept of the semicircle with the real axis of the Nyquist plot in Fig. 11 represented the alternating current equivalent series resistance, which was produced by a combination of the resistance of electrolyte, the internal resistance of active material and substrate, and the contact resistance at the active material–current collector interface [60]. The values were 0.56 Ω for 6 M KOH electrolyte and 1.21 Ω for 2 M $NaNO_3$ electrolyte. The radius of the semicircle represented pseudo-charge-transfer resistance [61]. Apparently, the resistive character in KOH electrolyte was relatively lower than that in $NaNO_3$ electrolyte

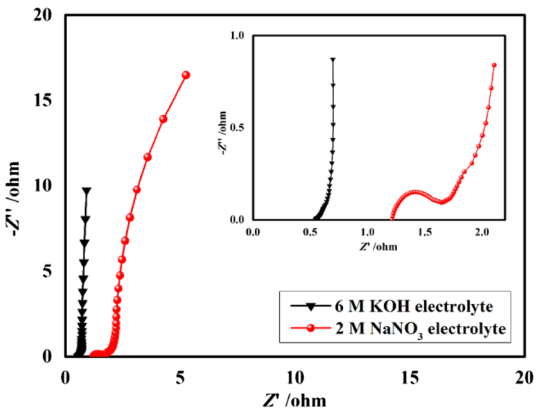

Fig. 11 Nyquist plot for CMG-800 sample (*Inset* shows the same in the higher frequency region)

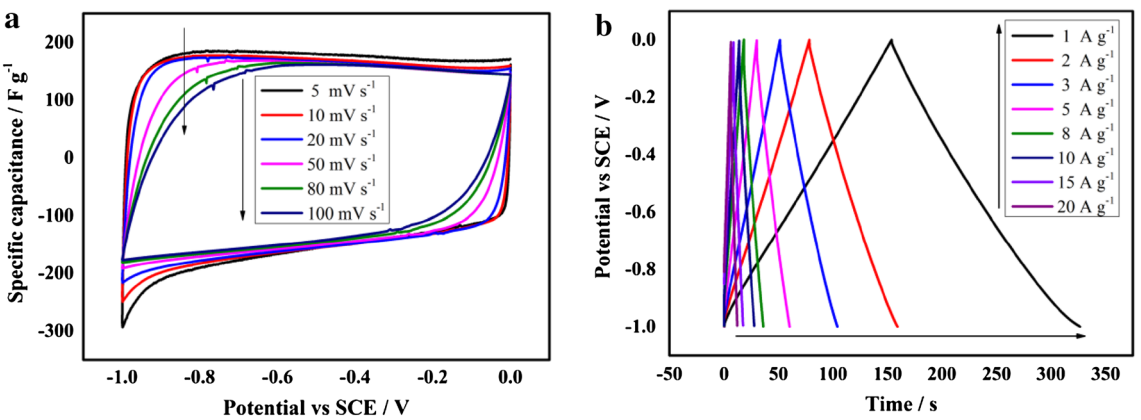

Fig. 10 **a** CV curves of CMG-800 sample in 2 M $NaNO_3$ at different current densities from 5 to 100 mV s^{-1}, and **b** GCD curve of CMG-800 sample at different current densities from 1 to 20 A g^{-1}

because of the larger size of solvated ions. Contrary to neutral aqueous solutions, the applied KOH electrolytes were characterized by high conductivity and low viscosity, accompanied by good charge propagation and power rates of capacitor, depending on the CMG-800 electrode materials. However, several drawbacks such as chemical etching existed.

4 Conclusion

Nitrogen-doped porous-carbon materials were successfully prepared from pure sodium glutamate by an easy method. The direct carbonization method described in this work was a one-step, efficient, economic, and environmentally benign synthesis strategy to produce nitrogen-doped porous carbons. The prepared nitrogen-doped porous-carbon materials showed a high BET specific surface area (1873 $m^2\ g^{-1}$), large pore volume (1.10 $cm^3\ g^{-1}$), and nitrogen content (5.08 at%). Favorable specific capacitances of 201 F g^{-1} in 6 M KOH solution and 174 F g^{-1} in 2 M $NaNO_3$ solution were achieved. These properties may enrich and broaden the use of nitrogen-doped porous carbons as electrodes, especially considering their high conversion rate, high surface area, and good electrochemical performance.

Acknowledgements This work was financially supported by the National Natural Science Foundation of China (NSFC, Nos. 21364004).

References

1. K. Chen, D. Xue, Rare earth and transitional metal colloidal supercapacitors. Sci. China Technol. Sci. **58** (11):1768–1778 (2015)
2. K. Chen, D. Xue, Ionic Supercapacitor electrode materials: a system-level design of electrode and electrolyte for transforming ions into colloids. Coll. Interface Sci. Commun. **1**, 39–42 (2014)
3. W. Gu, G. Yushin, Review of nanostructured carbon materials for electrochemical capacitor applications: advantages and limitations of activated carbon, carbide-derived carbon, zeolite-templated carbon, carbon aerogels, carbon nanotubes, onion-like carbon, and graphene. Wiley Interdiscip. Rev. Energy Environ. **3**(5), 424–473 (2014)
4. K. Chen, F. Liu, D. Xue, S. Komarneni, Carbon with ultrahigh capacitance when graphene paper meets $K_3Fe\ (CN)_6$. Nanoscale **7**(2), 432–439 (2015)
5. B. Yi, X. Chen, B. Zeng, K. Guo, Z. Wan, Q. Qian, H. Yan, J. Chen, Gelatin-based activated carbon with carbon nanotubes as framework for electric double-layer capacitors. J. Porous. Mater. **19**(1), 37–44 (2012)
6. K. Chen, D. Xue, Colloidal supercapacitor electrode materials. Mater. Res. Bull. **83**, 201–206 (2016)
7. K. Chen, S. Song, K. Li, D. Xue, Water-soluble inorganic salts with ultrahigh specific capacitance: crystallization transformation investigation of $CuCl_2$ electrodes. CrystEngComm. **15**(47), 10367–10373 (2013)
8. A.B. Fuertes, F. Pico, J.M. Rojo, Influence of pore structure on electric double-layer capacitance of template mesoporous carbons. J. Power Sources **133**(2), 329–336 (2004)
9. C. Sun, Y. Zhang, S. Song, D. Xue, Tunnel-dependent supercapacitance of MnO2: effects of crystal structure. J. Appl. Crystallogr. **46**(4), 1128–1135 (2013)
10. K. Chen, W. Pan, D. Xue, Phase transformation of Ce^{3+}-doped MnO_2 for pseudocapacitive electrode materials. J. Phys. Chem. C **120**(36), 20077–20081 (2016)
11. K. Chen, D. Xue, S. Komarneni, Colloidal pseudocapacitor: nanoscale aggregation of Mn colloids from MnCl 2 under alkaline condition. J. Power Sources **279**, 365–371 (2015)
12. K. Chen, D. Xue, High energy density hybrid supercapacitor: in-situ functionalization of vanadium-based colloidal cathode. ACS Appl. Mater. Interfaces **8**(43):29522–29528 (2016)
13. W. Du, R. Liu, Y. Jiang, Q. Lu, Y. Fan, F. Gao, Facile synthesis of hollow $Co_3\ O_4$ boxes for high capacity supercapacitor. J. Power Sources **227**, 101–105 (2013)
14. Y. Jiang, D. Chen, J. Song, Z. Jiao, Q. Ma, H. Zhang, L. Cheng, B. Zhao, Y. Chu, A facile hydrothermal synthesis of graphene porous NiO nanocomposite and its application in electrochemical capacitors. Electrochim. Acta **91**, 173–178 (2013)
15. F. Liu, D. Xue An electrochemical route to quantitative oxidation of graphene frameworks with controllable C/O ratios and added pseudocapacitances. Chemistry–A Eur. J. **19**(32):10716–10722 (2013)
16. K. Chen, S. Song, F. Liu, D. Xue, Structural design of graphene for use in electrochemical energy storage devices. Chem. Soc. Rev. **44**(17), 6230–6257 (2015)
17. K. Chen, F. Liu, S. Song, D. Xue, Water crystallization to create ice spacers between graphene oxide sheets for highly electroactive graphene paper. CrystEngComm. **16**(33), 7771–7776 (2014)
18. E. Ra, E. Raymundo-Piñero, Y. Lee, F. Béguin, High power supercapacitors using polyacrylonitrile-based carbon nanofiber paper. Carbon **47**(13), 2984–2992 (2009)
19. G. Lota, K. Fic, E. Frackowiak, Alkali metal iodide/carbon interface as a source of pseudocapacitance. Electrochem. Commun. **13**(1), 38–41 (2011)
20. Z. Wu, P.A. Webley, D. Zhao, Post-enrichment of nitrogen in soft-templated ordered mesoporous carbon materials for highly efficient phenol removal and CO_2 capture. J. Mater. Chem. **22**(22), 11379–11389 (2012)
21. Z. Lei, D. Bai, X. Zhao, Improving the electrocapacitive properties of mesoporous CMK-5 carbon with carbon nanotubes and nitrogen doping. Microporous Mesoporous Mater. **147**(1), 86–93 (2012)
22. K. Jurewicz, K. Babeł, A. Źiółkowski, H. Wachowska, Ammoxidation of active carbons for improvement of supercapacitor characteristics. Electrochim. Acta **48**(11), 1491–1498 (2003)
23. K. Jurewicz, R. Pietrzak, P. Nowicki, H. Wachowska, Capacitance behaviour of brown coal based active carbon modified through chemical reaction with urea. Electrochim. Acta **53**(16), 5469–5475 (2008)
24. Y. Liu, One-pot hydrothermal synthesis of nitrogen-doped hierarchically porous carbon monoliths for supercapacitors. J. Porous Mater. **21**(6), 1009–1014 (2014)
25. D-s Yuan, T-x Zhou, S-l Zhou, W-j Zou, Mo S-s, N-n Xia, Nitrogen-enriched carbon nanowires from the direct carbonization of polyaniline nanowires and its electrochemical properties. Electrochem. Commun. **13**(3), 242–246 (2011)
26. Y. Mao, H. Duan, B. Xu, L. Zhang, Y. Hu, C. Zhao, Z. Wang, L. Chen, Y. Yang, Lithium storage in nitrogen-rich mesoporous carbon materials. Energy Environ. Sci. **5**(7), 7950–7955 (2012)
27. F. Su, C.K. Poh, J.S. Chen, G. Xu, D. Wang, Q. Li, J. Lin, X.W. Lou, Nitrogen-containing microporous carbon nanospheres with

improved capacitive properties. Energy Environ. Sci. **4**(3), 717–724 (2011)
28. L. Zhao, L.Z. Fan, M.Q. Zhou, H. Guan, S. Qiao, M. Antonietti, M.M. Titirici, Nitrogen-containing hydrothermal carbons with superior performance in supercapacitors. Adv. mater. **22**(45), 5202–5206 (2010)
29. B. Xu, S. Hou, G. Cao, F. Wu, Y. Yang, Sustainable nitrogen-doped porous carbon with high surface areas prepared from gelatin for supercapacitors. J. Mater. Chem. **22**(36), 19088–19093 (2012)
30. L. Zhao, N. Baccile, S. Gross, Y. Zhang, W. Wei, Y. Sun, M. Antonietti, M.-M. Titirici, Sustainable nitrogen-doped carbonaceous materials from biomass derivatives. Carbon **48**(13), 3778–3787 (2010)
31. Y. Xia, R. Mokaya, Generalized and facile synthesis approach to N-doped highly graphitic mesoporous carbon materials. Chem. Mater. **17**(6), 1553–1560 (2005)
32. J.S. Lee, X. Wang, H. Luo, G.A. Baker, S. Dai, Facile ionothermal synthesis of microporous and mesoporous carbons from task specific ionic liquids. J. Am. Chem. Soc. **131**(13), 4596–4597 (2009)
33. M.D. Stoller, R.S. Ruoff, Best practice methods for determining an electrode material's performance for ultracapacitors. Energy Environ. Sci. **3**(9), 1294–1301 (2010)
34. B. Xu, H. Duan, M. Chu, G. Cao, Y. Yang, Facile synthesis of nitrogen-doped porous carbon for supercapacitors. J. Mater. Chem. A **1**(14), 4565–4570 (2013)
35. B. Xu, D. Zheng, M. Jia, G. Cao, Y. Yang, Nitrogen-doped porous carbon simply prepared by pyrolyzing a nitrogen-containing organic salt for supercapacitors. Electrochim. Acta **98**, 176–182 (2013)
36. D. Dollimore, P. Spooner, A. Turner, The BET method of analysis of gas adsorption data and its relevance to the calculation of surface areas. Surf. Technol. **4**(2), 121–160 (1976)
37. K.S. Walton, R.Q. Snurr, Applicability of the BET method for determining surface areas of microporous metal-organic frameworks. J. Am. Chem. Soc. **129**(27), 8552–8556 (2007)
38. Y. Wang, F. Su, C.D. Wood, J.Y. Lee, X.S. Zhao, Preparation and characterization of carbon nanospheres as anode materials in lithium-ion secondary batteries. Ind. Eng Chem. Res. **47**(7), 2294–2300 (2008)
39. K. Kakaei, Decoration of graphene oxide with Platinum Tin nanoparticles for ethanol oxidation. Electrochim. Acta **165**, 330–337 (2015)
40. A. Kajdos, A. Kvit, F. Jones, J. Jagiello, G. Yushin, Tailoring the pore alignment for rapid ion transport in microporous carbons. J. Am. Chem. Soc. **132**(10), 3252–3253 (2010)
41. A. Sadezky, H. Muckenhuber, H. Grothe, R. Niessner, U. Pöschl, Raman microspectroscopy of soot and related carbonaceous materials: spectral analysis and structural information. Carbon **43**(8), 1731–1742 (2005)
42. Y. Korenblit, M. Rose, E. Kockrick, L. Borchardt, A. Kvit, S. Kaskel, G. Yushin, High-rate electrochemical capacitors based on ordered mesoporous silicon carbide-derived carbon. Acs Nano **4**(3), 1337–1344 (2010)
43. R. Jansen, H. Van Bekkum, XPS of nitrogen-containing functional groups on activated carbon. Carbon **33**(8), 1021–1027 (1995)
44. A. Sánchez-Sánchez, F. Suárez-García, A. Martínez-Alonso, J.M. Tascón, Aromatic polyamides as new precursors of nitrogen and oxygen-doped ordered mesoporous carbons. Carbon **70**, 119–129 (2014)
45. Z. Lin, G. Waller, Y. Liu, M. Liu, C.P. Wong, Facile synthesis of nitrogen-doped graphene via pyrolysis of graphene oxide and urea, and its electrocatalytic activity toward the oxygen-reduction reaction. Adv. Energy Mater. **2**(7), 884–888 (2012)
46. D. Usachov, O. Vilkov, A. Gruneis, D. Haberer, A. Fedorov, V. Adamchuk, A. Preobrajenski, P. Dudin, A. Barinov, M. Oehzelt, Nitrogen-doped graphene: efficient growth, structure, and electronic properties. Nano Lett. **11**(12), 5401–5407 (2011)
47. L. Hao, X. Li, L. Zhi, Carbonaceous electrode materials for supercapacitors. Adv. Mater. **25**(28), 3899–3904 (2013)
48. S.B. Kulkarni, U.M. Patil, I. Shackery, J.S. Sohn, S. Lee, B. Park, S. Jun, High-performance supercapacitor electrode based on a polyaniline nanofibers/3D graphene framework as an efficient charge transporter. J. Mater. Chem. A **2**(14), 4989–4998 (2014)
49. V. Datsyuk, M. Kalyva, K. Papagelis, J. Parthenios, D. Tasis, A. Siokou, I. Kallitsis, C. Galiotis, Chemical oxidation of multiwalled carbon nanotubes. Carbon **46**(6), 833–840 (2008)
50. F. Ye, B. Zhao, R. Ran, Z. Shao, Facile mechanochemical synthesis of nano SnO2/graphene composite from coarse metallic Sn and graphite oxide: an outstanding anode material for lithium-ion batteries. Chemistry–A Eur J. **20**(14), 4055–4063 (2014)
51. D. Hulicova-Jurcakova, M. Seredych, G.Q. Lu, T.J. Bandosz, Combined effect of nitrogen-and oxygen-containing functional groups of microporous activated carbon on its electrochemical performance in supercapacitors. Adv. Funct. Mater. **19**(3), 438–447 (2009)
52. M. Thommes, K. Kaneko, A.V. Neimark, J.P. Olivier, F. Rodriguez-Reinoso, J. Rouquerol, K.S. Sing, Physisorption of gases, with special reference to the evaluation of surface area and pore size distribution (IUPAC Technical Report). Pure Appl. Chem. **87**(9–10), 1051–1069 (2015)
53. H. Luo, Y. Yang, X. Zhao, J. Zhang, Y. Chen, 3D sponge-like nanoporous carbons via a facile synthesis for high-performance supercapacitors: direct carbonization of tartrate salt. Electrochim. Acta **169**, 13–21 (2015)
54. H. Luo, Y. Yang, B. Mu, Y. Chen, J. Zhang, X. Zhao, Facile synthesis of microporous carbon for supercapacitors with a $LiNO_3$ electrolyte. Carbon **100**, 214–222 (2016). doi:10.1016/j.carbon.2016.01.004
55. B. Kishore, D. Shanmughasundaram, T.R. Penki, N. Munichandraiah, Coconut kernel-derived activated carbon as electrode material for electrical double-layer capacitors. J. Appl. Electrochem. **44**(8), 903–916 (2014)
56. X. Zhao, H. Luo, K. Du, F. Zhang, Y. Li, Application of attapulgite/maltose system on mesoporous carbon material preparation for electrochemical capacitors. J. Appl. Electrochem. **44**(6), 719–725 (2014)
57. Y. Wang, B. Chang, D. Guan, X. Dong, Mesoporous activated carbon spheres derived from resorcinol-formaldehyde resin with high performance for supercapacitors. J. Solid State Electrochem. **19**(6), 1783–1791 (2015)
58. X. Li, J. Wang, Y. Zhao, F. Ge, S. Komarneni, Z. Cai, Wearable solid-state supercapacitors operating at high working voltage with a flexible nanocomposite electrode. ACS appl. mater. interfaces **8**(39), 25905–25914 (2016)
59. M.D. Stoller, S. Park, Y. Zhu, J. An, R.S. Ruoff, Graphene-based ultracapacitors. Nano Lett. **8**(10), 3498–3502 (2008)
60. J. Zhang, X. Zhao, On the configuration of supercapacitors for maximizing electrochemical performance. ChemSus. Chem **5**(5), 818–841 (2012)
61. D. Hulicova, M. Kodama, H. Hatori, Electrochemical performance of nitrogen-enriched carbons in aqueous and non-aqueous supercapacitors. Chem. mater. **18**(9), 2318–2326 (2006)